26

Egypt. J. Chem. **59**, No. 4, pp. 445-464 (2016)

The Catalytic Performance of Fe_2O_3-CeO_2 Nanocomposite in Ethanol Conversion

W.A. Aboutaleb[a*], Heba M. Gobara[a], K.M. Hashim[a], Sohair A. Henein[a] and S.A. Hassan[b]

[a.]Egyptian Petroleum Research Institute, 1A Ahmed El-Zomor St. Naser City and [b]Ain-Shams University, 2 Gisr El-Swais St. Abbasia, Cairo, Egypt.

ETHANOL dehydration over Fe_2O_3-CeO_2 nanocomposite with different Fe_2O_3 wt % loadings was investigated. For comparison the pure Fe_2O_3 and CeO_2 were also prepared. The different nanocomposite samples were prepared via a novel modified co-precipitation method. Pure Fe_2O_3 and CeO_2 were prepared by conventional chemical precipitation method. The as-prepared catalysts were characterized by the aid of XRD, HRTEM, BET, TGA and XRF techniques. The results revealed that Fe_2O_3 and CeO_2 produce a solid solution up to 15% Fe_2O_3. In the samples of higher Fe_2O_3 content, segregation of Fe_2O_3 on the surface were evidenced. Catalytic conversion of ethanol yielded mainly dehydration products with a distinguished activity toward ethylene. The highest ethanol conversion and maximized ethylene selectivity were achieved on the $Fe_{15}Ce_{85}$ catalyst and its selectivity achieves 90%. While ethylene yield increased over all catalysts by increasing the reaction temperature, production of diethyl ether and acetaldehyde was favored at low temperatures with a minor yield.

Keywords: Ethanol, Fe_2O_3-CeO_2, Ethylene, Nanocomposite and Co-precipitation.

Ethanol is a renewable material produced by biomass fermentation with exciting transportation and storage infrastructure in many countries. Furthermore, there is an ascending annual production of bioethanol which exceeds 50 million tons per year. Recently, ethanol chemistry has attracted a great attention for production of many chemicals such as ethylene, ethyl acetate, acetaldehyde and hydrogen.

Ethylene is a basic feedstock for production of many petrochemicals such as poly-ethylene, ethylene oxide, ethylene dichloride and ethyl benzene. The ethanol catalytic dehydration is an attractive route for ethylene production since it overcomes the economical and by-products formation problems of cracking and oxidative dehydrogenation processes. Recently, ethanol catalytic dehydration was studied over many catalyst systems such as transition metal oxides[(1)], zeolites[(2–5)], silica–alumina[(6)], etc. Alumina has the major drawback of higher reaction temperatures and lower ethylene selectivities. Although zeolite based catalysts avoid the disadvantages of alumina, they suffer serious deactivation due to the cock formation[(7–10)].

*Corresponding author Email: waelepri2@yahoo.com, Tel: +2(02) 01015450148, Fax: +2(02)227727433.

On the other hand, α-Fe_2O_3 was reported as an attractive catalyst support or promoter for methanol and ethanol oxidation[11–13]. Among the few researchers who have considered α-Fe_2O_3 as an active phase for ethanol conversion to valuable products, Zaki *et al*.[1] investigated ethanol dehydration over mixed oxides containing Fe_2O_3. He claimed that the catalysts composed of iron–manganese oxides and of iron–manganese–silica oxides possess the highest selectivity due to the role of iron species reducibility in the oxidation processes. El-Katatny *et al*.[14] recovered hematite and alumina through aluminum industry and prepared Fe_2O_3/Al_2O_3 as catalyst for ethanol oxidation. They revealed that the active FeO_x/Al_2O_3 catalysts have good selectivity in ethanol dehydration into ethylene. Doping of Fe^{3+} with other metal oxides produced powerful hydroxyl radicals ($OH^{\cdot}$) as oxidizers[15, 16] that improve its photocatalytic activity.

On the other hand, ceria as metal oxide was extensively used as several noble metals supports and promoters for hydrogen production via ethanol oxidation [17,18]. It is an advantageous support due to its high oxygen storage capacity and mobility. Therefore, it improves the catalyst electronic and structural properties[19], enhance the noble metals reduction[20] and save the active metal particle size[21]. Additionally, it decreases the carbon formation on the catalyst surface[22].

The combination of the two reducible CeO_2–Fe_2O_3 mixed oxides enhances their chemical property that displays better catalytic activity than pure CeO_2 and pure α-Fe_2O_3 for many reactions[23-25]. Recently, CeO_2–Fe_2O_3 composite thin film was investigated as a highly active and sensitive alcohols sensor[26]. A very recent communication has shown that Au/CeO_2–Fe_2O_3 nanocomposite is an active agent for methanol oxidative steam reforming[27] . However, no results were published for CeO_2–Fe_2O_3 composite oxides as catalyst for the ethanol dehydration.

The pure α-Fe_2O_3, CeO_2 and Fe-doped CeO_2 have been synthesized by many techniques such as hydrothermal[28], spray pyrolysis[29], sol-gel[30], gas condensation[31], sonochemical[32] and precipitation methods[33]. Considering the performance of Au/Fe_2O_3, Au/CeO_2 and CeO_2–Fe_2O_3 composite in the CO and methanol oxidation and sensing, we proposed that the Ce–Fe mixed oxides could be suitable catalyst for ethanol dehydration. Therefore, the objective of the present work is to prepare the CeO_2–Fe_2O_3 nanocomposites and investigate their catalytic activity in ethanol dehydration. The nanocomposite composition impact on their catalytic behavior was evaluated by varying the Fe/(Ce + Fe) ratio.

Experimental

Catalyst preparation

Cerium nitrate hexahydrate $Ce(NO_3)_3{\cdot}6H_2O$ and Ferric nitrate nonahydrate $Fe(NO_3)_3{\cdot}9H_2O$ were used as precursors to precipitate CeO_2 and Fe_2O_3 respectively, while, ammonia solution was used as the precipitating agent.

For ceria nanoparticles preparation, a 0.1 M cerium nitrate hexahydrate precursor was dissolved in 1 liter of distilled water. During this time, the color of solution changed from purple to yellow. The ammonium hydroxide solution (33%) was then continuously added dropwisely to the reaction vessel at room temperature until pH=11. The precipitated solid was then aged by keeping the solution under energetic stirring for 120 min at 60-70° C. Addition of ammonia caused the solution to go purple once again; however after the solution aging a turbid yellow suspension was produced. Afterwards, the suspension was allowed to settle and to cool down to 30° C before being filtered. The precipitate was filtered, washed 5 times with distilled water to ensure the ammonia solution removal. The resulting solids were dried at 120° C for about 4 hr. The dried solids were powdered to allow an even calcination and to assist the fast removal of the evolved gases. The dried solids were transformed into metal oxides by calcination at 300° C for 3 hr. The furnace was heated up and cooled down by a temperature ramp of 10° C/ min. The product was more dense yellowish powder. In the same manner, iron oxide nanoparticles were prepared by precipitation. A 0.1 M Ferric nitrate nonahydrate $Fe(NO_3)_3 \cdot 9H_2O$ was dissolved in 1 liter distilled water. The solution was stirred by a magnetic stirrer and heated up to 50° C. A 33% ammonium hydroxide solution was then added slowly until the pH=11 was reached. The precipitate was stirred for further 3 hr and was then filtered and washed with distilled water 5 times. Afterwards, the solids were dried for 4 hr at 120° C and calcined at 400° C for 3 hr.

A series of ceria-hematite nanocomposite with different Fe/Ce ratios was prepared using the co-precipitation method in two steps as follows:

The desired amount of cerium nitrate was dissolved in 1 liter distilled water and precipitated as mentioned before. The solution was evaporated to get the precipitate which was dried at 120° C for 4 hr. The dried cerium hydroxide was then suspended with vigorous stirring in iron nitrate solution of the appropriate concentration corresponding to the desired Fe/Ce percent. Ammonium hydroxide solution was then added dropwise at the room temperature to produce the required nanocomposite. The solution color turned reddish violet. The precipitate was filtered, washed 5 times with distilled water and finally dried at 200° C for 4 h and calcined at 300° C for 3 hr.

Catalysts characterization

X-ray diffraction (XRD)

The structure and different phases of prepared pure metal oxides and nanocomposites were investigated via the XRD technique. The XRD patterns of all samples were recorded by X-ray X'Pert powder diffractometer (Philips, D8-Brucker Model), equipped with Ni filter and Cu kα-radiation (λ= 1.5418 Å) at 40 kV and 30 mA. The samples were scanned using Bragg's configuration in 2θ range from 10° to 80° with 0.04° s-1 scanning rate. Before measurements, the samples were grounded manually to fine powder. The mean crystalline size DXRD was calculated with Scherer's equation:

$$D = K\lambda / \beta \cos \theta$$

where, the spherical model is assumed for the grains, K equals 0.9, λ is the wavelength of X-ray radiation (λ=1.5418 Å), B is the peak full width at half maximum (FWHM) and θ is the angle of diffraction.

Transmission electron microscopy (TEM)

The morphology and the average particle sizes of all samples under study were investigated by using high resolution TEM apparatus (JEOL), JEM 2100 Electron microscope at 120 Kw with 600,000 magnifications, Japan, attached with (EDX) Oxford X-Max. The catalyst samples were ground using an agate mortor before testing. 0.1 gm of ground samples was suspended in 10 ml ethyl alcohol. One droplet of suspended solution was set on copper holder coated with thin film of carbon (of mesh size 200 μm) and was left to dry for 2 hr. It was then put on TEM column in the path of electron beam and the images were taken at the selected power of magnification.

BET surface area

The different surface parameters of the solid materials were determined from N_2 adsorption-desorption isotherms measured at -196^{o}C using a NOVA 3200 apparatus, USA. The as-synthesized ceria and nanocomposite samples were initially out-gassed under vacuum (10^{-4} Torr) at 200^{o}C for 24 hr, whereas, Fe_2O_3 were pre-heated at 150^{o}C for 24 hr. The BET-surface areas (S_{BET}) were calculated from the adsorption branch by the aid of BET equation using multi –points method at relative pressure P/Po = 0.05-0.3. Pore size distributions (PSD) were calculated using Barrett, Joyner and Halenda (BJH) method from desorption branch of the isotherms. The particle sizes (D_{BET}) were calculated from the BET surface area (S_{BET}) values using the following relationship, assuming spherical particles model:

$$D_{BET} = 6/ \rho S_{BET},$$

where, ρ is the theoretical density of the powder (viz., 7.13 g/cm^3 for CeO_2 and 5.242 g/cm^3 for Fe_2O_3). The degree or extent of agglomeration of the powder particles was evaluated from D_{BET}/D_{XRD}.

Thermal analysis (TGA)

Thermogravimetric (TG)-differential scanning calorimetry (DSC) and differential thermal analysis (DTA) of all prepared nanocatalysts were carried out using simultaneous DSC-TGA SDTQ 600, USA under N_2 atmosphere, with a heating rate of 10^o C min^{-1} in the room temperature - 1000° C range.

X-ray fluorescence (XRF)

The elemental composition of the samples was determined by X-ray fluorescence (XRF) spectrometry in a P-analytical AXIOS PW4400 spectrophotometer with Rh tube as a source of radiation. The measurements were performed onto pressed pellets containing 6 wt % wax.

Temperature programmed reduction (TPR)

TPR experiments were carried out on an automatic multitask unit RIG-100 from ISRI equipped with a thermal conductivity detector (TCD) with output to a computer. The catalyst (40 mg) was placed in the reactor and purged with UHP Ar at room temperature and then the TPR measurement was performed using 10 % H_2/He gas mixture. The temperature was increased at a rate of 10° C/ min from the room temperature up to 1000 ◦C. The effluent gas was passed through silica gel to remove water before measuring the amount of hydrogen consumed during the reduction by the TC detector.

Catalytic activity

Catalytic activity of CeO_2, α -Fe_2O_3 nanocatalysts and a series of α-Fe_2O_3-CeO_2 nanocomposites prepared by co-precipitation technique was tested through ethanol conversion as a model reaction using a micro catalytic pulse technique attached to data acquisition. The first part was used to supply the needed N_2 gas to vaporize the ethanol. The reactor effluent was passed through a chromatographic column for separation and determination of the products using flame ionization detector (FID) connected to a computerized data acquisition station. The column of 200 cm length and 0.3 cm internal diameter was used containing acid-washed PW chromosorb (60-80 μm mesh size) loaded by 15% by weight squalane. The reactions were carried out under atmospheric pressure in the temperature range, 250 – 450° C. H_2 flow rate was kept constant at 50 ml min^{-1}. In a micro catalytic reactor, 0.20 g of the dried catalyst was placed between two thin quartz layers. Prior to catalytic activity runs, the reduced catalyst samples were heated in N_2 flow for 2 hr at 450° C for activation. Few doses of reactants were injected first to reach the steady state of the reaction. The temperature of the chromatographic column was adjusted and controlled at 60° C.

Catalytic activity and selectivity calculations

The catalytic activity experiments for ethanol conversion were expressed in the terms of yield, total conversion and % selectivity calculated as follows[34]: Ethanol conversion (wt%) = Σ yield% of each component in the products Component yield (wt%) = quantity of the component/total quantity of the produced components. Fractional selectivity of each component = yield (wt%)/ total conversion x 100

Results and Dissections

XRD analysis

Figure 1 illustrates the XRD patterns of the as prepared CeO_2, Fe_2O_3 and different Fe_2O_3-CeO_2 loaded samples. The XRD pattern of pure CeO_2 shows a high intensity peak at 2θ = 28.5° characteristic of ceria (111) fluorite structure. However, the other lower intensity peaks at 33.08, 47.47, 56.33, 59.08, 69.40, 76.69, and 79.067 are assigned for some other CeO_2 lattice structures[35]. The diffractions in Fig.1b reveal strong peaks at 2θ = 3.18 and 35.86 which are attributed to α-Fe_2O_3 phase. The obtained patterns showed neither γ-Fe_2O_3 nor

Fe_3O_4 peaks in the iron oxide sample which ensured the formation of pure hematite particles. As hematite was loaded to ceria, only the ceria peaks were detected, which have become broader and with lower intensities. This change in ceria peaks can be attributed to incorporation of Fe^{+3} into the ceria lattice to form $Fe_xCe_{1-x}O_2$ solid solution[36]. Recently, the formation of $Fe_xCe_{1-x}O_2$ solid solution prepared through the wet route under mild conditions was reported[36,37]. Moreover, by loading Fe^{+3} to ceria lattice, the peaks were shifted to higher 2θ values, which may confirm the formation of the solid solution, considering the smaller Fe^{3+} ionic radius (0.67 Å) compared to that of Ce^{4+} (0.102 Å) [38, 39].

Furthermore, the iron oxide patterns assigned for $Fe_{30}Ce_{70}$ and $Fe_{50}Ce_{50}$ sample point to the ceria lattice distortion. This effect was also reported by Neri *et al.*[40]. He claimed that by annealing the Fe-Ce samples at low calcination temperatures, the presence of ceria inhibited the hematite formation. However, annealing the samples above 600 °C led to separate hematite and ceria phases. It is worth mentioning that, the appearance of α-Fe_2O_3 phase for the $Fe_{50}Ce_{50}$ sample in our work may be attributed to the applied preparation conditions which seem favorable for Fe^{3+} segregation rather than the substitution of Ce^{4+} in the cubic cell. These results are consistent with Laguna *et al.* suggesting that 25% iron content is the solubility limit of iron in ceria matrix[41]. Bao *et al.* have also reported that the substitution of Ce^{4+} by Fe^{3+} mechanism in the ceria lattice depends on the concentration of loaded iron ions[42]. Doping with lower amount of Fe^{3+} (~10 mol. %) facilitates the formation of oxygen vacancies whereas doping with a large amount of Fe^{3+} annihilates the oxygen.

As well, the average particle sizes of CeO_2, Fe_2O_3 and composites were calculated from the corresponding (111) and (110) diffraction peaks, respectively, using Scherrer equation. The obtained values are included in Table 1.

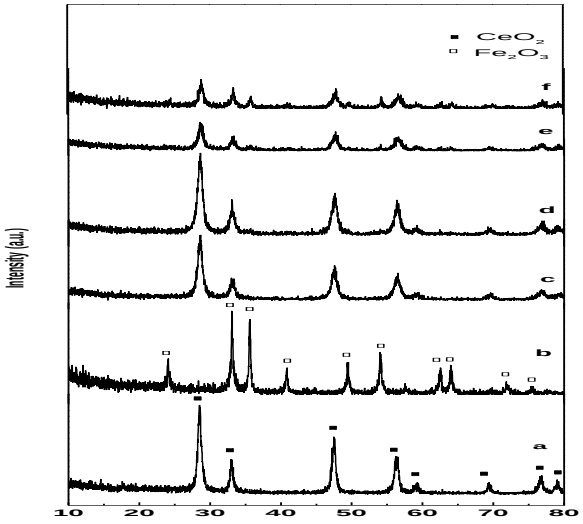

Fig. 1. XRD patterns of the a) pure CeO_2, b) pure Fe_2O_3, c) Fe_5Ce_{95}, d) $Fe_{15}Ce_{85}$, e) $Fe_{30}Ce_{70}$, f) $Fe_{50}Ce_{50}$.

TABLE 1. The calculated particle size from the XRD patterns.

Composites with nominal Fe_2O_3 ratios (%)	XRD Results		Surface characteristics			
	a_o [a] (Å)	D_{XRD} [b] (nm)	S_{BET} (m^2/g)	D_{BET} [c] (nm)	V_P (cm^3/g)	r_p (nm)
CeO_2	5.399	34.7	100.547	8.37	0.2009	3.997
5% Fe_2O_3/ CeO_2	5.389	41.7	113.876	7.39	0.2134	3.748
15% Fe_2O_3 / CeO_2	5.399	13.0	125.388	7.23	0.2145	3.577
30% Fe_2O_3/ CeO_2	5.385	11.9	119.450	7.05	0.2052	4.003
50% Fe_2O_3/ CeO_2	5.359	10.5	79.906	10.53	0.1905	4.069
α-Fe_2O_3	4.69	105.4	57.249	19.99	0.1860	2.496

TEM investigation

Figure 2 depicts the TEM images for the prepared Fe-Ce solid nanocomposites as well as pure ceria and hematite as well. The pure iron oxide prepared in this work by the mentioned precipitation method appeared as porous nanorods with average sizes ranged between 11 and 15 nm (Fig. 2, a). The prepared pure ceria was shown as uniformly distributed cubic nanocrystallites with an average size of 10-13 nm (Fig. 2, b). From the TEM analysis of nanocomposite with different Fe/Ce percent (Fig. 2, c-f), the iron oxide appeared as small black spots, which were rather homogeneously distributed on the ceria. With increasing the iron oxide loading in the composite, the black spots were increased (observed as average of many positions in the images). This result confirms that the catalysts under this study were well-mixed. Also, the cubic CeO_2 crystallite size was decreased with increasing the Fe_2O_3 loading, while the crystallite size of Fe_2O_3 was not much changed. The mean particle size of ceria in the nanocomposites with Fe/Ce ratio of 5, 15, 30 and 50 were 7, 5.5, 4.2 and 3.2, respectively. For $Ce_{50}Fe_{50}$ catalyst, the large hexagonal shaped nanoparticles and nanorods of α-Fe_2O_3 (marked with arrows in Fig. 2, f) were uniformly dispersed on the ceria surface particles. This observation ensured that separate iron oxide particles were formed at ceria surface on $Ce_{50}Fe_{50}$ sample. Hence, there was a limit to mix the oxides as cited in literature[23, 43]. The iron oxide particle size distribution obtained by measuring the sizes of 100 particles indicated a narrow particle size distribution; viz., in the range among the measured particles of 45-48 nm. These results run in agreement with the XRD analysis which showed diffractions for only α-Fe_2O_3 in the $Ce_{50}Fe_{50}$ catalyst. Additionally, it may explain the larger surface area and lower catalytic activity of this catalyst sample than those of the $Ce_{70}Fe_{30}$ one.

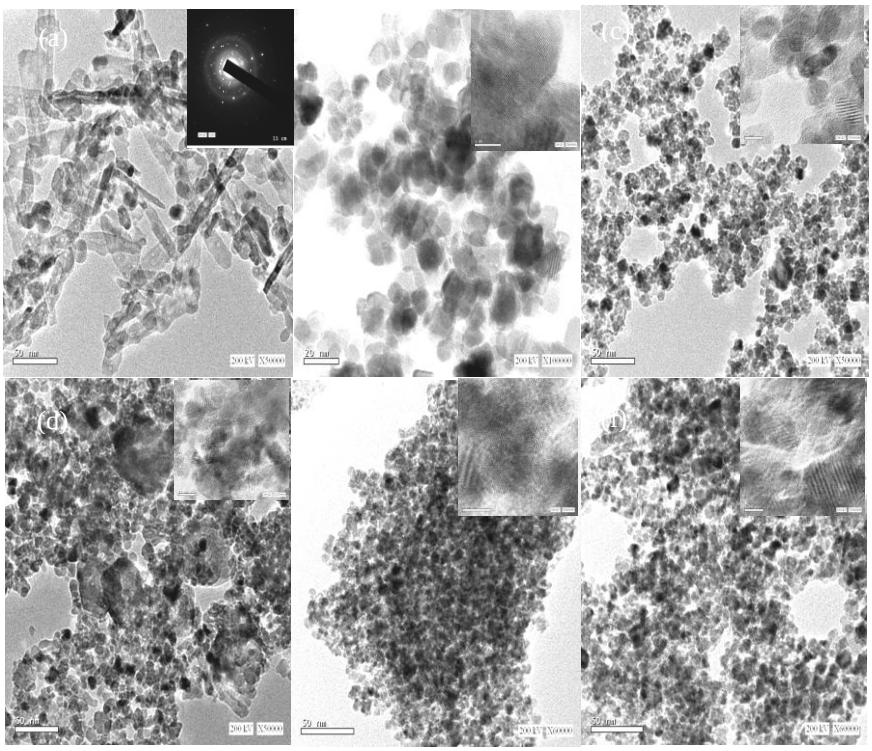

Fig. 2. TEM micrograph of a) pure Fe_2O_3, b) pure CeO_2, c) Fe_5Ce_{95}, d) $Fe_{15}Ce_{85}$, e) $Fe_{30}Ce_{70}$, f) $Fe_{50}Ce_{50}$, Insets show the corresponding diffraction patterns of the samples.

Textural characteristics

The specific surface area and average pore size of the prepared catalysts were measured from the adsorption branch of the isotherms as reported in Table 1. The obtained isotherms are illustrated in Fig. 3. The BET results have shown a strong influence on specific surface area by varying the catalyst composition (Table 1). For instance, as the Fe concentration in the mixed oxide nanocomposites was increased, a significant decrease in catalyst S_{BET} was observed except for the $Fe_{30}Ce_{70}$ sample. The surface areas of pure CeO_2 and pure Fe_2O_3 were measured as 100.574 and 57.249 m^2/g, respectively. The Fe_2O_3- CeO_2 composites had higher specific surface areas than that of CeO_2 up to $Fe_{15}Ce_{85}$ sample which revealed the highest specific surface area of 125.338 m^2/g compared to all catalysts under this study. Such S_{BET} change trend was in agreement with Perez-Alonso *et al*.[24] which reported that Fe–Ce nanocomposites, prepared by co-precipitation method with calcination at 300 °C, possess higher specific areas than those of pure CeO_2 and Fe_2O_3. However, the specific surface areas of $Ce_{30}Fe_{70}$ and $Ce_{50}Fe_{50}$ nanocomposite decreases up to 79.9 m^2/g, due to the segregation of Fe_2O_3 segregation rather than the substitution of Ce^{4+} in the cubic cell. This behaviour seems to be too close to that one of the same composition in Ref.[25].

Figure 3a and b shows the N_2 adsorption-desorption isotherms for the studied catalysts and their corresponding pore size distributions. The obtained isotherms were similar for all catalysts, demonstrating the intermediate properties of Type IV isotherms characteristic for mesoporous materials. Moreover, type H2 hysteresis loop at high relative pressure was exhibited for all catalysts under study, related mainly to the capillary condensation within mesoporous structures [(43)]. This type of pores related to ink-bottel type of pores with narrow neck and wide orifice. Additionally, the sharp curvature in P/Po from 0.55 to 0.95 observed in all cases revealed that CeO_2 has promoted the mesoporous structure of Fe_2O_3 phase. The pore size distribution curve showed that pore size of both CeO_2 and Fe_2O_3 are nearly 4 nm, which shifted to lower value with increasing the content Fe up to $Ce_{30}Fe_{70}$ which preserved the pore size of the pure CeO_2. For $Ce_{50}Fe_{50}$ creation of micropores in addition to a wide pore size distribution curve were observed (Fig. 3b, f).

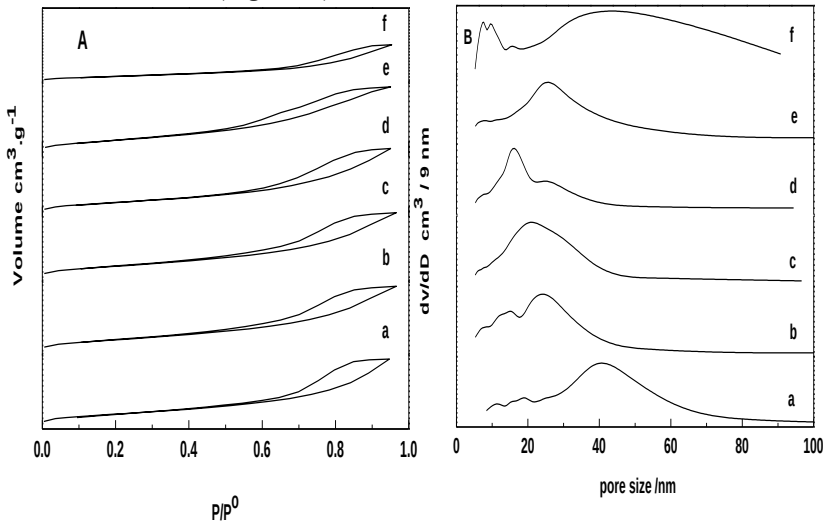

Fig. 3. N_2 adsorption–desorption isotherms and BJH pore volume of a) pure CeO_2, b) Fe_2O_3, c) Fe_5Ce_{95}, d) $Fe_{15}Ce_{85}$, e) $Fe_{30}Ce_{70}$, f) $Fe_{50}Ce_{50}$.

XRF analysis

The XRF technique was used to determine the actual metal loading percent and the composition of Fe_2O_3-CeO_2 nanocomposites calcined at 300 °C. The results are summarized in Table 2. The results showed that all the doped samples have iron contents close to the targeted values. Similar results have been reported for mixed oxides synthesized by the same method, indicating that the thermal decomposition of the propionates promotes the interaction of the cations enhancing the homogeneity of the obtained solid[(44)].

TABLE 2. Actual Fe mole percent of the prepared Fe_2O_3-CeO_2 nanocomposites measured by XRF technique .

Catalysts	Actual Fe mole%	Fe/(Ce+Fe)
Fe_5Ce_{95}	5.13	5%
$Fe_{15}Ce_{85}$	15.56	15%
$Fe_{30}Ce_{70}$	28.05	30 %
$Fe_{50}Ce_{50}$	52.04	50%

Thermo-gravimetric analysis

The obtained TGA curves for all the catalysts used are shown in Fig. 4. The results indicated two stages of weight loss during the heating ramp from 35 to 1000 °C. The first weight loss observed up to about 100 °C for all samples was attributed to the removal of physically adsorbed water. Another weight loss stage was assigned in the temperature range of 100–450 °C for CeO_2 and Fe_2O_3-CeO_2 samples. This weight loss might be corresponding to the oxidation of carbonaceous species from citric acid. The Fe_2O_3 sample exhibited the highest thermal stability with only 3% weight loss before 320^o C, while a monotonic weight decrease proceeds for this sample in the range from 450 up to 650 °C. Generally, the extent of weight loss for the studied samples showed the descending order as: $Fe_{30}Ce_{70}$> $Fe_{15}Ce_{85}$ > CeO_2> Fe_5Ce_{95}> $Fe_{50}Ce_{50}$> Fe_2O_3.

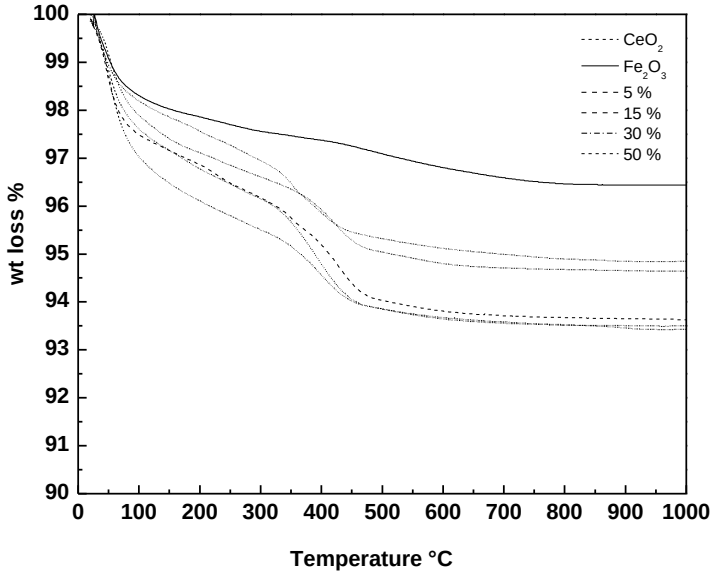

Fig. 4. TGA profile of a) pure Fe_2O_3, b) pure CeO_2, c) Fe_5Ce_{95}, d) Fe_{15} Ce_{85}, e) $Fe_{30}Ce_{70}$, f) $Fe_{50}Ce_{50}$.

Temperature programmed reduction (TPR)

The reduction profiles of the prepared samples were investigated by the TPR technique as presented in Fig. 5. Generally, the CeO_2 reduction profile (Fig. 5, a) provided two peaks: one at ca. 500° C and the other (broad) above 800 °C. These peaks are commonly attributed to the ceria lattice surface and bulk oxygen reduction, respectively[44]. In our results, a broad peak was detected at a temperature around 340 °C, which might be referred to the low-temperature reducibility of CeO_2 due to its small particle size[3]. On the other hand, the TPR profile of the pure Fe_2O_3 (Fig. 5, e) showed three strong peaks at ca. 438, 700 and 800 °C, being attributed to the stepwise reduction of α-Fe_2O_3 to metallic iron[2]. As stated in literature, α-Fe_2O_3 is reduced firstly to magnetite at a temperature around 400 °C, whereas magnetite is converted to FeO at higher temperature, viz., 700 °C, then with increasing the temperature up to 900 °C, the FeO is converted to Fe^0 [4, 20, 24]

The reduction behavior of the samples with different iron content is depicted in Fig. 5, b-d. The obtained profiles reveal that, as the iron content is lowered, a greater shift is observed to lower temperature in the assigned reduction peak of Fe_2O_3 at 438° C. This observation may be explained by the close interaction between Fe and Ce cations, due to the formation of hematite-like solid solution[24]. This observation confirms the XRD data for Fe-Ce mixed oxide samples. Moreover, the observed peak shift may suggest that the CeO_2 loading enhances the Fe_2O_3 surface reducibility through a permanent interface formation, since their interaction increases the H_2 adsorption at lower temperature[45].

It is worth mentioning that, the sample Fe_5Ce_{95} exhibited the strongest influence of CeO_2 on Fe_2O_3 reducibility. The peak at 340 °C detected for pure ceria declined to be broader with increasing the Fe loading. This may be attributed to the increase in CeO_2 particle size and/or it can be related to the reduction of CeO_2 surface oxygen at lower temperature in presence of Fe_2O_3.

It is known that the iron ions loading to the ceria cubic cell slightly influences the reduction of surface cerium. Several researches have reported a broad shoulder at low temperature range for all mixed CeO_2–Fe_2O_3 supports profiles. This shoulder was suggested to be assigned to the reduction of ceria surface oxygen.

Finally, one can conclude that, the synergism between cerium and iron oxide produces a mixed oxide with relatively high reducibility at lower temperature.

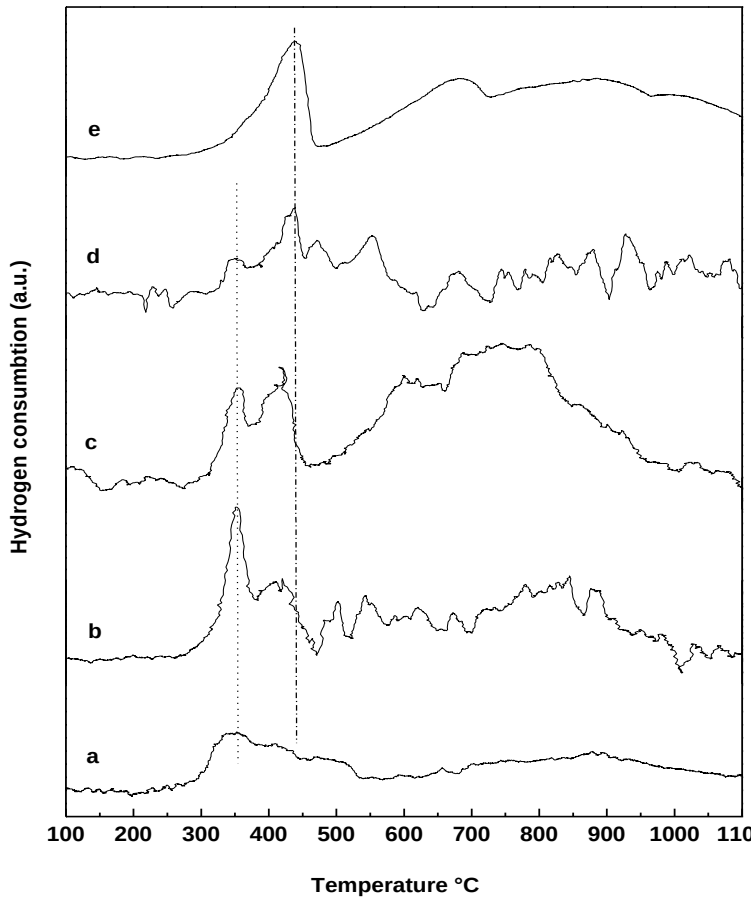

Fig. 5. The TPR profile of samples a) CeO_2, b) Fe_5Ce_{95}, c) $Fe_{15}Ce_{85}$, d) $Fe_{30}Ce_{70}$ and e) pure Fe_2O_3.

Catalytic activity

The effect of Fe content as well as the reaction temperature on the ethanol conversion under nitrogen atmosphere is illustrated in Fig. 6. As shown, the ethanol conversion values are increased with increasing the reaction temperatures from 250 to 450 °C over all the studied catalysts achieving 100 % conversion at 450°C. There is an abrupt increase in the total conversion at temperature ≥ 350 °C, this behavior may be related to the activation of the catalysts at higher reaction temperatures. The conversion% over the nanocomposites under this study as well as the neat Fe_2O_3 and the CeO_2 being arranged in the following order: $Fe_{15}Ce_{85}$ > Fe_2O_3 > Fe_{30} Ce_{70} > $Fe_{50}Ce_{50}$ > Fe_5Ce_{95} > CeO_2.

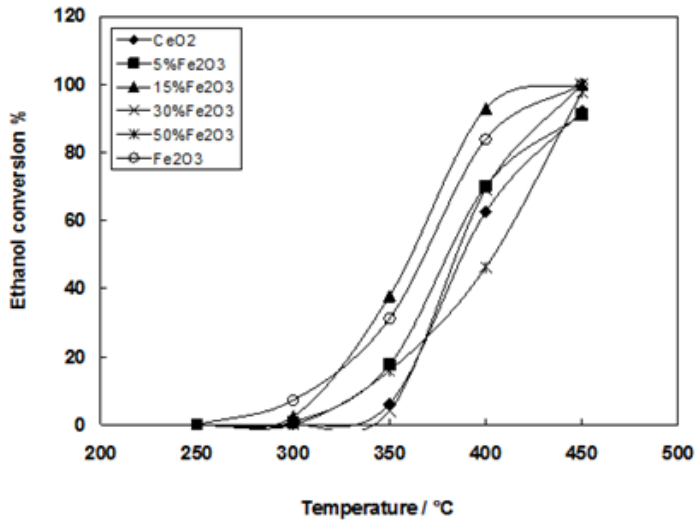

Fig. 6. Effect of reaction temperature on ethanol conversion over the pure Fe_2O_3, CeO_2 and Fe_2O_3-CeO_2 nanocomposites.

All catalyst samples under study exhibited the main activity in the temperature range of 250-450 °C toward production of ethylene, *i.e*., toward dehydration pathway of the reaction. This was accompanied with much lower activity toward acetaldehyde production (dehydrogenation pathway). Additionally, minor products such as diethyl ether together with a lower yield of acetaldehyde were detected in the chromatographic column.

Figure 7 shows the catalytic activity towards ethylene production as a function of the reaction temperature and Fe content in the composites. The ethylene yield (mole %) and the selectivity (%) to ethylene show an increase by increasing the reaction temperature. Generally, the Fe-contained catalysts show higher ethylene yields than pure CeO_2, keeping a satisfactory ethanol conversion level until the end of the test, indicating the positive effect of Fe_2O_3 incorporation. The $Fe_{15}Ce_{85}$ sample exhibits the highest yield (85.8 %) and % selectivity (90 %) 450^{o}C among all the composite samples under this study, this may be due to the highest surface area of this sample compared to the other samples. By further increase of Fe loading to CeO_2, the obtained ethylene yield decreases. This behaviour seems to be the favorable Fe^{3+} segregation rather than the substitution of Ce^{4+} in the cubic cell as clearly evidenced from XRD results. The neat CeO_2 and Fe_2O_3 showed also a reasonable catalytic activity towards ethylene production where the yield (mole %) is 60 and 77 % at 450^{o}C for pure CeO_2 and Fe_2O_3, respectively. The temperature at which the maximum ethylene yield obtained is higher over Fe-Ce compared with CeO_2 or Fe_2O_3 oxides alone. Moreover, the change in activity trend for ethylene production could be attributed to the reduced coke formation observed over the mixed oxide catalyst.

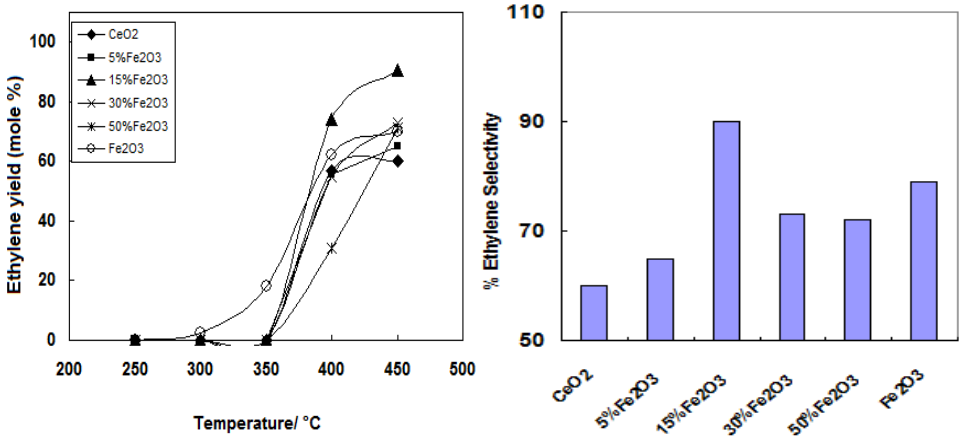

Fig. 7. Ethylene yield (mole %) as a function of reaction temperature over the prepared catalysts.

It is well known that the basic and acidic properties of the oxide catalysts are essential parameters directly affecting the primary selectivity for ethylene or acetaldehyde. Basic sites are predominant in the ethanol dehydrogenation to acetaldehyde, whereas ethylene would be produced with an essential role of the acidic sites of the oxides[46]. It worth mentioning that Riad *et al.*[45] and T. Zaki[1] have reported relatively high dehydration activities for catalysts containing iron oxide at the higher reaction temperatures; *e.g.*, 500° C. Such high activity was explained in view of the presence of brönsted acid sites. It is to be mentioned that incorporation of Fe_2O_3 is responsible for creating the brönsted acid sites which in turn can enhance the dehydration pathway of ethanol into ethylene.

On the other hand, Fig. 8 shows the formation of a minor quantity of acetaldehyde over all catalysts under study at different reaction temperatures. The maximum acetaldehyde yield was observed over $Ce_{15}Fe_{85}$ catalyst which reached 23.1 % at 350° C. In all cases, its yield increases up to 350° C and then decreased at the higher temperatures (> 350° C) due to the formation of other products.

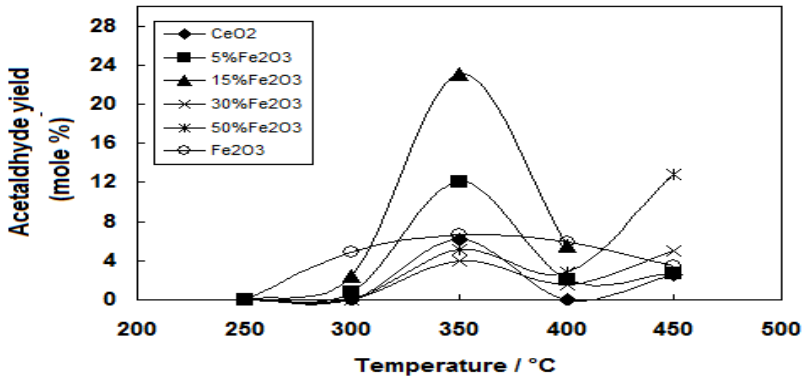

Fig. 8. Effect of reaction temperature on acetaldehyde yield (mole %) over the prepared catalysts.

The formation of diethyl ether (DEE) as an intermolecular dehydration product was investigated and illustrated in Fig. 9. The results revealed that the catalytic performance for diethyl ether formation over all catalysts almost related to those of ethylene formation (Fig. 7). All catalysts showed a low yield of DEE and the maximum yield was 15.8 **%** at 400°C over pure Fe_2O_3. The yield increases with reaction temperature till 350° C or 400°C then decreases at higher temperature due to formation of other products.

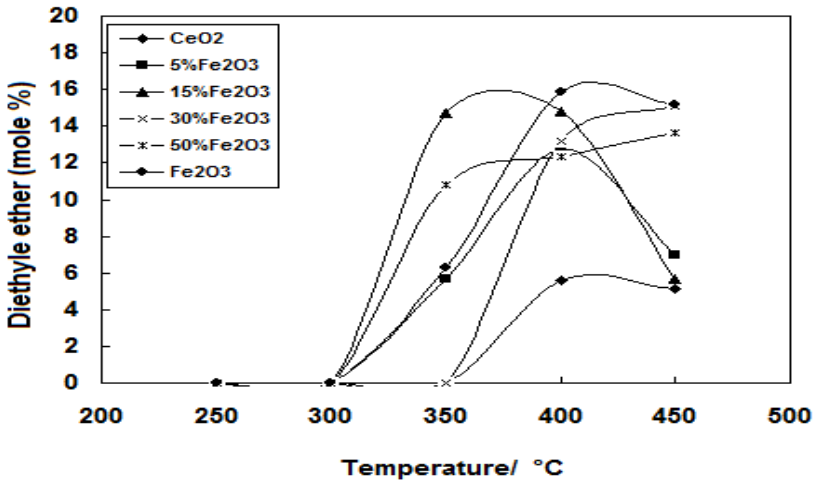

Fig. 9. Effect of reaction temperature on diethyl ether yield (mole %) over the prepared catalysts.

For ethanol dehydration mechanism, it is known that after ethanol adsorption on the acid centers of the catalyst surface where an oxonium ion ($C_2H_5OH_2^+$) formed, which might react with another C_2H_5OH molecule to form the diethyl ether or dehydrates to form the ethylene[47]. Those abilities to form either product depend basically on the surface site acidity. Whereas, at low surface acidity, the ethanol adsorption strength on the acid sites diminished so that C_2H_5–O bond becomes stronger that preferred intermolecular reaction[48]. Also, Phung *et al.* proposed the possibility of second ethanol molecule activation nearest the acido-basic sites over SiO_2-Al_2O_3 catalysts which could be beneficial for DEE formation[49].

Conclusions

A novel method was used to produce the Fe_2O_3–CeO_2 nanocomposites as well as the neat CeO_2 and α-Fe_2O_3. All catalyst samples under this study exhibited a high thermal stability up to 1000°C. Porous α-Fe_2O_3 nanorods and Flourite structure of CeO_2 could be produced by precipitation method. The results proved the Fe_2O_3 segregation with the increase of Fe loading over 15%. The synergism between cerium and iron oxide produces a mixed oxide with relatively high reducibility at lower temperatures. The catalytic activity results revealed that Fe_2O_3–CeO_2 nanocomposites with different Fe content (5–50 wt %) were promising catalysts for ethanol dehydration into ethylene. All the prepared

catalysts showed a high selectivity to ethylene. A low yield of both acetaldehyde and diethyl ether was observed in the chromatographic column. It was shown that the catalytic properties of Fe_2O_3–CeO_2 catalysts are related to oxygen vacancies and the active surface site acidity. The high activity to ethylene formation over $Fe_{15}Ce_{85}$ catalyst was attributed to the high surface area and limited ability of Fe-Ce solid solution formation with higher Fe% loading. The catalytic activity towards ethylene production revealed that all catalysts under this investigation showed remarkable activity and $Fe_{15}Ce_{85}$ catalyst sample is the most active and selective catalyst which achieves max yield of 85.8% and selectivity of 90%. The nanocomosites materials synthesized throughout this work are active and selective candidates for production of ethylene from ethanol.

References

1. **Zaki. T.,** Catalytic dehydration of ethanol using transition metal oxide catalysts. *J Colloid Interface Sci.* **284,** 606-613 (2005).

2. **Xiao, Y., Li, X., Yuan, Z., Li, J. and Chen, Y.**, Catalytic dehydration of ethanol to ethylene on TiO_2/4A zeolite composite catalysts. *Catal Lett.* **130**, 308-311 (2009).

3. **Wu, L-P., Li, X-J., Yuan, Z-H. and Chen, Y.**, The fabrication of TiO_2-supported zeolite with core/shell heterostructure for ethanol dehydration to ethylene. *Catal Commun.* **11**, 67-70 (2009).

4. **Zhang, X., Wang, R., Yang, X. and Zhang, F.**, Comparison of four catalysts in the catalytic dehydration of ethanol to ethylene. *Microporous Mesoporous Mater.* **116**, 210-215 (2008).

5. **Zhang, D., Wang, R. and Yang, X.**, Effect of P content on the catalytic performance of P-modified HZSM-5 catalysts in dehydration of ethanol to ethylene. *Catal Lett.* **124**, 384-391 (2008).

6. **Takahara, I., Saito, M., Inaba, M. and Murata, K.**, Dehydration of ethanol into ethylene over solid acid catalysts. *Catal Lett.* **105**, 249-252 (2005).

7. **Gayubo, A.G., Aguayo, A.T., Tarrío, A.M., Olazar, M. and Bilbao, J.,** Kinetic modelling for deactivation by coke deposition of a HZSM-5 zeolite catalyst in the transformation of aqueous ethanol into hydrocarbons. *Stud. Surf. Sci. Catal.* **139**, 455-462 (2001).

8. **Aguayo, A.T., Gayubo, A.G., Atutxa, A., Olazar, M. and Bilbao, J.,** Catalyst deactivation by coke in the transformation of aqueous ethanol into hydrocarbons. Kinetic modeling and acidity deterioration of the catalyst. *Ind. Eng. Chem. Res.* **41**, 4216-4224 (2002).

9. **Aguayo, A.T., Gayubo, A.G., Atutxa, A., Valle, B. and Bilbao, J.,** Regeneration of a HZSM-5 zeolite catalyst deactivated in the transformation of aqueous ethanol into hydrocarbons. *Catal Today.* **107**, 410-416 (2005).

10. **Gayubo, A.G., Alonso, A., Valle, B., Aguayo, A.T. and Bilbao, J.,** Selective production of olefins from bioethanol on HZSM-5 zeolite catalysts treated with NaOH. *Appl Catal B.* **97**, 299-306 (2010).

11. **Chang, F-W., Yu, H-Y., Roselin, L.S., Yang, H-C. and Ou, T-C.,** Hydrogen production by partial oxidation of methanol over gold catalysts supported on TiO_2-MO_x (M= Fe, Co, Zn) composite oxides. *Appl Catal A.* **302**, 157-167 (2006).

12. **Chang, F-W., Roselin, L.S. and Ou, T-C.,** Hydrogen production by partial oxidation of methanol over bimetallic Au-Ru/Fe_2O_3 catalysts. *Appl Catal A.* **334**, 147-155 (2008).

13. **Litt, G. and Almquist, C**., An investigation of CuO/Fe_2O_3 catalysts for the gas-phase oxidation of ethanol. *Appl Catal B.* **90**,10-17 (2009).

14. **El-Katatny, EA., Halawy, SA., Mohamed, M.A. and Zaki, M.I.,** Recovery of ethene-selective FeO_x/Al_2O_3 ethanol dehydration catalyst from industrial chemical wastes. *Appl Catal A.* **199**, 83-92 (2000).

15. **Channei, D., Inceesungvorn, B., Wetchakun, N., Phanichphant, S., Nakaruk, A., Koshy, P. and Sorrell, C.C.,** Photocatalytic activity under visible light of Fe-doped CeO_2 nanoparticles synthesized by flame spray pyrolysis. *Ceram Int.* **39**, 3129-3134 (2013).

16. **An, H., Li, J., Zhou, J., Li, K., Zhu, B. and Huang, W.,** Iron-coated TiO_2 nanotubes and their photocatalytic performance. *J. Mater. Chem.* **20**, 603-610 (2010).

17. **Silva, A.M., Costa, L.O.O., Barandas, A., Borges, L.E.P. and Mattos, L.V., Noronha, F.B,** Effect of the metal nature on the reaction mechanism of the partial oxidation of ethanol over CeO_2-supported Pt and Rh catalysts. *Catal Today*. **133**, 755-761 (2008).

18. **Mattos, L.V. and Noronha, F.b.B.**, Partial oxidation of ethanol on supported Pt catalysts. *J. Power Sources,* **145**, 10-15 (2005).

19. **Piras, A., Trovarelli, A. and Dolcetti, G.,** Remarkable stabilization of transition alumina operated by ceria under reducing and redox conditions. *Appl Catal B.* **28**, L77-L81 (2000).

20. **Trovarelli, A.,** Catalytic properties of ceria and CeO_2-containing materials. *Catal Rev*. **38**, 439-520 (1996).

21. **Cai, W., Wang, F., Zhan, E., Van Veen, A.C., Mirodatos, C. and Shen, W.**, Hydrogen production from ethanol over Ir/CeO_2 catalysts: A comparative study of steam reforming, partial oxidation and oxidative steam reforming. *J. Catal.* **257**, 96-107 (2008).

22. **Wang, S. and Lu, G.Q.M.,** Role of CeO_2 in Ni/$CeO_2Al_2O_3$ catalysts for carbon dioxide reforming of methane. *Appl Catal B.* **19**, 267-277 (1998).

23. **Li, K., Wang, H., Wei, Y. and Liu, M.,** Preparation and characterization of $Ce_{1-x}Fe_xO_2$ complex oxides and its catalytic activity for methane selective oxidation. *J. Rare Earths*, **26**, 245-249 (2008).

24. **Pérez-Alonso, F.J. and Melián-Cabrera, I., Granados, M.L., Kapteijn F., Fierro, JLG**, Synergy of $Fe_xCe_{1-x}O_2$ mixed oxides for N_2O decomposition. *J Catal.* **239**, 340-346 (2006).

25. **Pérez-Alonso, FJ., López Granados, M., Ojeda, M., Terreros, P., Rojas, S., Herranz, T., Fierr,o J.L.G., Gracia, M. and Gancedo, J.R.,** Chemical structures of coprecipitated Fe-Ce mixed oxides. *Chem Mater.* **17**, 2329-2339 (2005).

26. **Neri, G., Bonavita, A., Rizzo, G., Galvagno, S., Capone, S. and Siciliano, P.,** A study of the catalytic activity and sensitivity to different alcohols of $CeO_2Fe_2O_3$ thin films. *Sens Actuators B.* **111**, 78-83 (2005).

27. **Satitthai, U., Luengnaruemitchai, A. and Gulari, E.,** Effect of gold loading on CeO_2-Fe_2O_3 for oxidative steam reforming of methanol. *Inter. J. Chem. Molec. Nucl. Mater. and Metallur. Eng.* **6** (4), 305-310 (2012).

28. **Masui, T., Hirai, H., Imanaka, N., Adachi, G., Sakata, T. and Mori, H.,** Synthesis of cerium oxide nanoparticles by hydrothermal crystallization with citric acid. *J. Mater. Sci. Lett.* **21**, 489-491 (2002).

29. **Elidrissi, B., Addou, M., Regragui, M., Monty, C., Bougrine, A. and Kachouane, A.,** Structural and optical properties of CeO_2 thin films prepared by spray pyrolysis. *Thin Solid Films*, **379**, 23-27 (2000).

30. **Phonthammachai, N., Rumruangwong, M., Gulari, E., Jamieson, A.M., Jitkarnka, S. and Wongkasemjit, S.,** Synthesis and rheological properties of mesoporous nanocrystalline CeO_2 via sol-gel process. *Colloids Surf A.* **247**, 61-68 (2004).

31. **Guillou, N., Nistor, L.C., Fuess, H. and Hahn, H.,** Microstructural studies of nanocrystalline CeO_2 produced by gas condensation. *Nanostruct. Mater.* **8**, 545-557 (1997).

32. **Yin, L., Wang, Y., Pang, G., Koltypin, Y. and Gedanken, A.,** Sonochemical synthesis of cerium oxide nanoparticles-effect of additives and quantum size effect. *J. Colloid Interface Sci.* **246**, 78-84 (2002).

33. **Chen, H-I. and Chang, H-Y.,** Homogeneous precipitation of cerium dioxide nanoparticles in alcohol/water mixed solvents. *Colloids Surf A.* **242**, 61-69 (2004).

34. **Hassan, S.A., Gobara, H.M., Gomaa, M.M., Mohamed, R.S. and Khalil, F.H.,** Can microwave assisted in situ reduction of supported Pt nanoparticles challenge the chemical method in controlling the dispersion profile catalytic performance relationship? *RSC Adv.* **5**, 54460-54470 (2015).

35. **Kunming, J.I.A., Zhang, H. and Wencui, L.I.,** Effect of Morphology of the Ceria Support on the Activity of Au/CeO_2 Catalysts for CO Oxidation. *Chin. J. Catal.* **29**, 1089-1092 (2008).

36. **Hongyan, L.I.N., Zhiqiang, M.A., Ling, D., Jieshan, Q.I.U. and Liang, C.,** Preparation of nanoscale $Ce_{1-x}Fe_xO_2$ solid solution catalyst by the template method and Its catalytic properties for ethanol steam reforming. *Chin. J. Catal.* **29**, 418-420 (2008).

37. **Li, G., Smith R.L. and Inomata, H., S**ynthesis of nanoscale $Ce_{1-x}Fe_xO_2$ solid solutions via a low-temperature approach. *J. Am. Chem. Soc.* **123**, 11091-11092 (2001).

38. **Wang, W-C., Chen, S-Y., Glans, P-A., Guo, J., Chen, R-J., Fong, K-W. Chen, C-L., Gloter A., Chang C-L. and Chan, T-S.**, Towards understanding the electronic

structure of Fe-doped CeO_2 nanoparticles with X-ray spectroscopy. *Phys. Chem. Chem. Phys.* **15**, 14701-14707 (2013).

39. **Tabakova, T., Avgouropoulos, G., Papavasiliou, J., Manzoli, M., Boccuzzi, F., Tenchev, K., Vindigni, F. and Ioannides, T.,** CO-free hydrogen production over Au/CeO_2-Fe_2O_3 catalysts: Part 1. Impact of the support composition on the performance for the preferential CO oxidation reaction. *Appl Catal B.* **101**, 256-265 (2011).

40. **Neri, G., Bonavita, A., Rizzo, G., Galvagno, S., Capone, S. and Siciliano, P.,** Methanol gas-sensing properties of CeO_2-Fe_2O_3 thin films. *Sens Actuators B.* **114**, 687-695 (2006).

41. **Laguna, O.H., Centeno, M.A., Arzamendi, G., Gandía, L.M., Romero-Sarria, F. and Odriozola, J.A.,** Iron-modified ceria and Au/ceria catalysts for total and preferential oxidation of CO (TOX and PROX). *Catal Today.* **157**, 155-159 (2010).

42. **Bao, H., Chen, X., Fang, J., Jiang, Z. and Huang, W.,** Structure-activity relation of Fe_2O_3-CeO_2 composite catalysts in CO oxidation. *Catal Lett.* **125**, 160-167 (2008).

43. **Lowell, S., Shields, JE., Thomas, MA. and Thommes, M.,** Characterization of porous solids and powders: surface area, pore size and density. *Springer Sci. Bus. Media*. (2012).

44. **Romero-Sarria, F., Vargas, J.C., Roger, A-C. and Kiennemann, A.,** Hydrogen production by steam reforming of ethanol: Study of mixed oxide catalysts $Ce_2Zr_{1.5}Me_{0.5}O_8$: Comparison of Ni/Co and effect of Rh. *Catal Today,* **133**, 149-153 (2008).

45. **Riad, M., Sobhi, Z. and Mikhail, S.,** Catalytic dehydration reaction of ethanol Over transition metal catalysts. *J. Eng. Appl. Sci.* **49,** 195-208 (2002).

46. **Haryanto, A., Fernando, S., Murali, N. and Adhikari, S.,** Current status of hydrogen production techniques by steam reforming of ethanol: A review. *Energy Fuels*, **19**, 2098-2106 (2005).

47. **El-Salaam, KMA. and Hassan, EA.,** Active surface centres in a heterogeneous CdO catalyst for ethanol decomposition. *Surf. Technol.* **16**, 121-128 (1982).

48. **Golay, S., Kiwi-Minsker, L., Doepper, R. and Renken, A.,** Influence of the catalyst acid/base properties on the catalytic ethanol dehydration under steady state and dynamic conditions. In situ surface and gas-phase analysis. *Chem. Eng. Sci.* **54**, 3593-3598 (1999).

49. **Phung, T.K. and Busca, G.,** Diethyl ether cracking and ethanol dehydration: Acid catalysis and reaction paths. *Chem. Eng. J.* **272**, 92-101 (2015).

(*Received* 6 /3 /2016;
accepted 23 /3/ 2016)

الأداء العالى لحافز أكسيد الحديد – اكسيد السيريوم ذات جزيئات النانو المتراكبة فى عملية تحويل الكحول الايثيلى

وائل أبو طالب، هبه جبارة ، كرم محمد هاشم، سهير عياد و صلاح عبده*

معهد بحوث البترول و *كلية العلوم – جامعة عين شمس – القاهرة – مصر.

يعتبر انتاج غاز الاثيلين من نزع الماء من الايثانول من العمليات الصناعية الهامة وفي هذا البحث تمت هذه العملية بنجاح بافراز الايثانول على متراكب نانو من اكسيد الحديد و السيريوم ويزيد معدل انتاج غازالاثيلين بهذه الطريقة الجيديدة فى درجات الحرارة العالية أما في درجات الحرارة المنخفضة فيتكون خليط من داى اثيل ايثر والأسيتالدهيد بكميات منخفضة.